Available online at www.sciencedirect.com
SCIENCE DIRECT®
Journal of Sound and Vibration 265 (2003) 1003–1023
JOURNAL OF SOUND AND VIBRATION
www.elsevier.com/locate/jsvi

Vibration analysis of the tension shadow mask with wire impact damping

Sung-Dae Kim[a], Won-Jin Kim[b], Chong-Won Lee[a,*]

[a] *Department of Mechanical Engineering, Center for Noise and Vibration Control (NoViC), Korea Advanced Institute of Science and Technology, Science Town, Daejeon 305-701, South Korea*
[b] *Faculty of Mechanical and Automotive Engineering, Keimyung University, Taegu, 704-701, South Korea*

Received 7 May 2002; accepted 19 August 2002

Abstract

Non-linear vibration of the CRT shadow mask with impact damping wires is analyzed in consideration of the mask tension distribution and the effect of wire impact damping. A reduced order FEM model of the shadow mask is obtained from dynamic condensation of the mass and stiffness matrices, and damping wire is modelled using the lumped parameter method to effectively describe its contact interactions with the shadow mask. The non-linear contact–impact model is composed of spring and damper elements, of which parameters are determined from the Hertzian contact theory and the restitution coefficient, respectively. The analysis model of the shadow mask with damping wires is experimentally verified through impact tests of shadow masks performed in a vacuum chamber. Using the validated analysis model of the shadow mask with damping wires, the 'design of experiments' technique is applied to search for the optimal damping wire configuration so that the vibration attenuation of the shadow mask is maximized.

1. Introduction

The cathode ray tube (CRT) for computer monitors or TV sets is composed of a glass envelope and its inner parts. Among these parts, the shadow mask plays an important role in the CRT; it filters red, green and blue (RGB) electron beams emitted from electron gun to fit the desired RGB phosphors on the screen. Excessive vibrations of the shadow mask subject to external disturbances may thus lead to landing shifts of the electron beams from the desired phosphors, deteriorating the color purity of the picture on the screen. This is called the microphonic phenomenon, which is an undesirable characteristic of the CRT.

*Corresponding author. Tel.: +82-42-869-3016; fax: +82-42-869-8220.
E-mail address: cwlee@novic.kaist.ac.kr (C.-W. Lee).

0022-460X/03/$ - see front matter © 2002 Published by Elsevier Science Ltd.
doi:10.1016/S0022-460X(02)01241-5

Shadow masks are classified into two groups depending upon the manufacturing method: the press-formed and tension types. Among them, the tension type shadow mask has been developed mainly for large CRTs because of its durable stiffness characteristics against deformation. However, it exhibits a very light damping effect in the vacuum environment. Once a tension shadow mask is disturbed by an impulsive shock, the resulting vibration usually lasts for 1 or 2 min. To effectively attenuate such prolonged vibration, adjustment of tension distribution of the shadow mask and use of additional damping equipment are widely adopted in practice.

The V-shaped tension distribution, with large tension at both ends and small tension at the shadow mask center, and the M-shaped tension distribution have been attempted to enhance the vibration reduction efficiency of the tension shadow mask [1,2]. However, it has been found that the microphonic phenomenon is not sufficiently prevented by adjustment of the tension distribution alone, requiring additional damping mechanism for the tension shadow mask.

Among others, damping wire is known to be a good candidate for such damping mechanism, although there are some drawbacks such as the difficulty in assembling and the presence of its shadow on the screen. This study is mainly concerned with the vibration analysis of the tension shadow mask with damping wires.

The majority of previous works, which are mostly patents, on the vibration analysis of the tension shadow mask with damping wires have relied on experimental methods. Ohmura [3] experimentally evaluated the effects of damping wires on the vibration of an aperture grille tension shadow mask, showing that the vibration is reduced but it is transferred to the neighboring grilles. A vibration reduction method for the shadow mask was also proposed through adjustment of the shadow mask curvature in order to maximize the contact force between damping wire and shadow mask in the regions of interest [4].

Many patents including Ref. [5] discussed the role of damping wire fixture in the vibration attenuation, relying on experimental methods and inventor's intuition. There have been only a few analytical studies on the effects of damping wires on the vibration characteristics of the shadow mask. For example, Shin [6] attempted to analyze the vibration characteristics of a simple flat shadow mask with constant tension distribution and damping wires using a commercial FEM code, but the simulation results were not in good agreement with the experiments, mainly due to poor modelling of the contact mechanism.

In this work, the vibration of the curved shadow mask with V-shaped tension distribution, as shown in Fig. 1, is analyzed in consideration of the effect of wire impact damping. First of all, we develop a reduced order dynamic model of the shadow mask with V-shaped tension distribution using a commercial FEM code and the dynamic condensation method, and a lumped-parameter model of the damping wire. In the dynamic condensation process, the nodes of wire models are chosen so that they match with the nodes of the condensed mask model and thus the contact interaction between the wires and the mask surface can be conveniently described. The contact mechanism between the damping wire and the shadow mask plate is modelled as a non-linear contact–impact model composed of spring and damper elements of which parameters are determined from the Hertzian contact theory and the restitution coefficient, respectively. For the sake of the computational efficiency as well as accuracy, the deduced impact stiffness coefficient is further reduced in the simulations.

The analysis model of the shadow mask with damping wires is experimentally verified through impact tests of shadow masks performed in a vacuum chamber. Using the validated analysis

model of the shadow mask with damping wires, the 'design of experiments' technique is applied to search for the optimal damping wire configuration so that the vibration attenuation of the shadow mask is maximized.

2. Modelling of the shadow mask

2.1. Fe analysis of the tension shadow mask

Consider the typical commercial shadow mask shown in Fig. 1, which has V-shaped tension distribution along the x-axis. Shadow mask for CRT is a thin steel plate with the array of small holes, of which the shape and size are determined by some rules. Fig. 2 shows the typical array of holes of a slit shadow mask. It is impractical, if not impossible, to analyze a full mask FE model accounting for the accurate shape and size of the whole array of holes, since a mask has millions

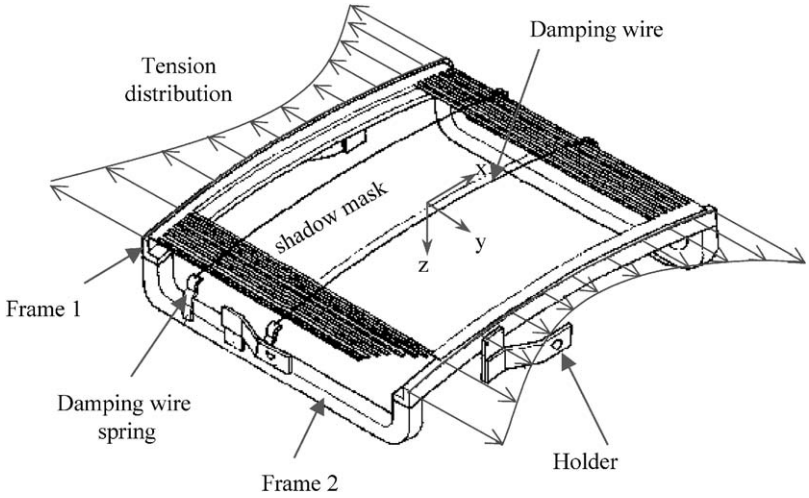

Fig. 1. Tension shadow mask with damping wires.

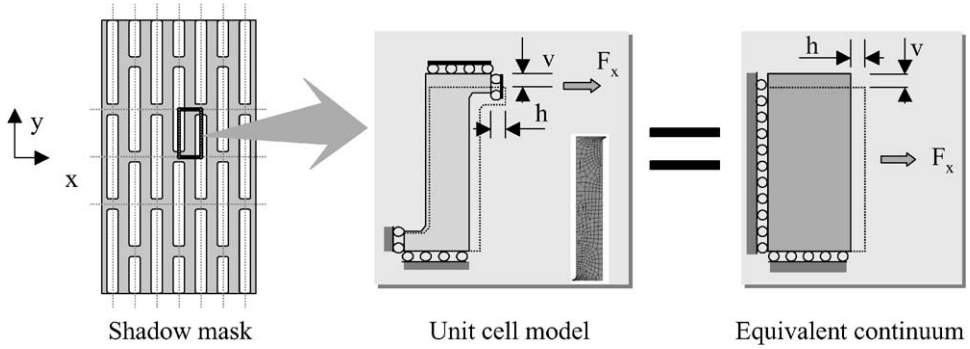

Fig. 2. Extraction of effective material properties using unit cell model.

of holes. For the efficiency of analysis, an anisotropic continuum plate model without holes has been commonly adopted, introducing the effective material properties extracted from the original plate model [7]. The effective material properties can be calculated from the analysis of unit cell model of the original shadow mask under proper boundary conditions, as shown in Fig. 2. When symmetric forces are imposed to a real continuum plate, the deformed shape of a very small rectangular element remains as a rectangle, which is used for boundary conditions of the unit cell model. The effective material properties in the x, y directions are then obtained as [7]

$$E_x = \frac{\sigma_x}{\varepsilon_x} = \frac{(F_x/\mathrm{d}y\,\mathrm{d}z)}{h/\mathrm{d}x} \qquad v_{yx} = \frac{\varepsilon_y}{\varepsilon_x} = \frac{v/\mathrm{d}y}{h/\mathrm{d}x},$$
$$E_y = \frac{\sigma_y}{\varepsilon_y} = \frac{(F_y/\mathrm{d}x\,\mathrm{d}z)}{v/\mathrm{d}y} \qquad v_{xy} = \frac{\varepsilon_x}{\varepsilon_y} = \frac{h/\mathrm{d}x}{v/\mathrm{d}y}, \tag{1}$$

where the subscripts x and y represent the x and y directions, respectively; E is the Young's modulus and σ is the normal stress; ε and v are the normal and the shear strains, respectively; $\mathrm{d}x$, $\mathrm{d}y$ and $\mathrm{d}z$ are the undeformed element dimensions of the unit cell model in the x, y and z directions, respectively; and, h and v are the deformations of the unit cell model in the x and y directions due to the loadings F_x andF_y, respectively.

Table 1 compares the original and effective material properties of the tested shadow mask of interest. Fig. 3 and Table 2 compares the measured and computed modes of the tested shadow mask without damping wires, which are in good agreement with each other. Note that each mode tends to be localized along the x direction. Higher modes are pushed away from the plate center towards the ends where the tension is higher. This fact is well confirmed in Fig. 4, which compares the dominant natural frequency distribution of the tested shadow mask without damping wires along the x position obtained from experiments and FE analysis.

2.2. Dynamic condensation of mass and stiffness matrices

There are too many degrees of freedom in a full FE model of the shadow mask to effectively conduct the non-linear vibration analysis of the shadow mask with damping wires, requiring dynamic condensation of the full FE shadow mask model without damping wires. Since the shadow mask mainly vibrates along the z direction, the degrees of freedom in the z direction are chosen as the master degrees of freedom and the others as the slave degrees of freedom [8].

Table 1
The original and effective material properties of the shadow mask

	Original	Effective	Ratio (%)
E_x (N/mm^2)	2.1×10^5	4.220×10^2	0.2
E_y (N/mm^2)		1.567×10^5	74.6
v_{xy}	0.3	0.41	137
v_{yx}		0.000698	0.23
Density (kg/mm^3)	7.80×10^{-6}	5.95×10^{-6}	76.3
Nominal dimension	$610 \times 460 \times 0.1$ mm^3		

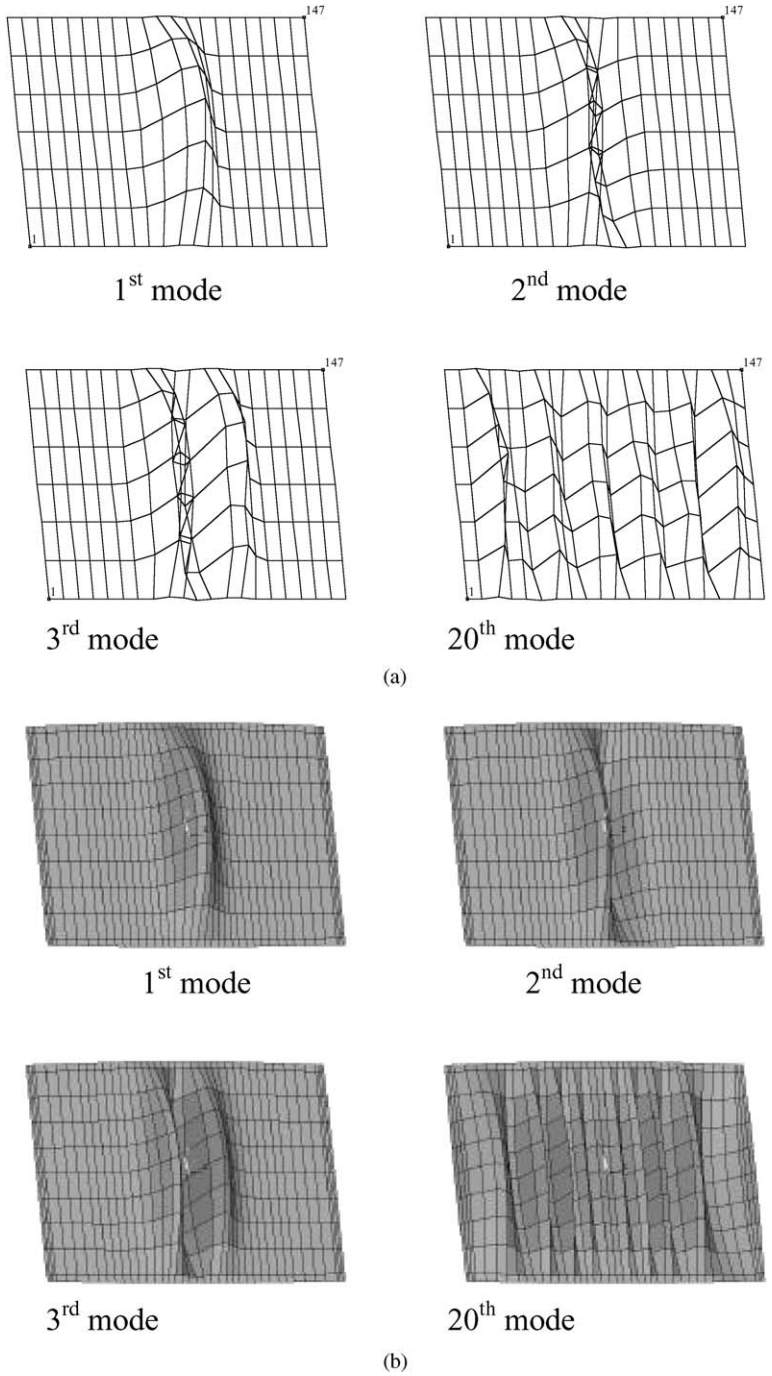

Fig. 3. Comparison of mode shapes obtained from (a) experiments and (b) FE analysis.

Table 2
Natural frequencies of the shadow mask without damping wires

Mode	1st	2nd	3rd	20th
Full model	106.3	111.1	115.7	180.3
Condensed model	106.5	111.6	116.5	189.2
Measured	106	111	116	188

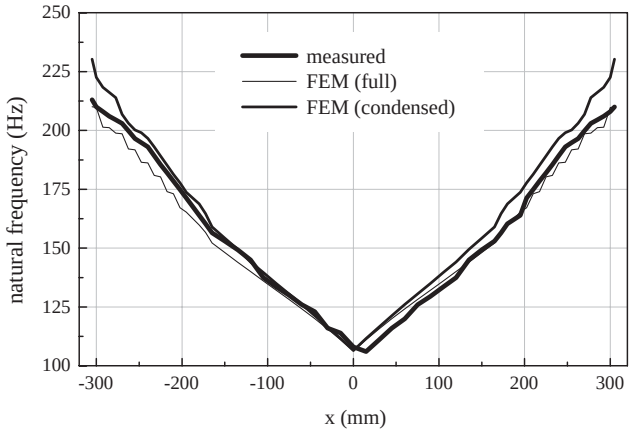

Fig. 4. Dominant natural frequency distribution.

The equation of motion of the tension shadow mask is obtained, using the FEM, as

$$\mathbf{M}_0\ddot{\mathbf{u}} + \mathbf{K}_0\mathbf{u} = \mathbf{0}, \tag{2}$$

where $\mathbf{M}_0$ and $\mathbf{K}_0$ are the mass and the stiffness matrices, respectively. The co-ordinate vector $\mathbf{u}$, of which degrees of freedom is six times the number of nodes, can be partitioned into the retained vector, $\mathbf{u}_m$, and the eliminated vector, $\mathbf{u}_s$, which are associated with the master and slave degrees of freedom, respectively. Note that the retained vector, $\mathbf{u}_m$, corresponds to the z directional co-ordinate vector, of which degrees of freedom is one sixth of $\mathbf{u}$. Partitioning $\mathbf{M}_0$ and $\mathbf{K}_0$ in a compatible manner, Eq. (2) becomes

$$\begin{bmatrix} \mathbf{M}_{mm} & \mathbf{M}_{ms} \\ \mathbf{M}_{sm} & \mathbf{M}_{ss} \end{bmatrix} \begin{Bmatrix} \ddot{\mathbf{u}}_m \\ \ddot{\mathbf{u}}_s \end{Bmatrix} + \begin{bmatrix} \mathbf{K}_{mm} & \mathbf{K}_{ms} \\ \mathbf{K}_{sm} & \mathbf{K}_{ss} \end{bmatrix} \begin{Bmatrix} \mathbf{u}_m \\ \mathbf{u}_s \end{Bmatrix} = \mathbf{0}. \tag{3}$$

The second row of Eq. (3) can be reduced to, assuming that the relationship between $\mathbf{u}_s$ and $\mathbf{u}_m$ is not significantly affected by the inertia effect,

$$\mathbf{K}_{sm}\mathbf{u}_m + \mathbf{K}_{ss}\mathbf{u}_s = \mathbf{0} \qquad \text{or} \qquad \mathbf{u}_s = -\mathbf{K}_{ss}^{-1}\mathbf{K}_{sm}\mathbf{u}_m. \tag{4}$$

Thus we obtain the relationship given by

$$\mathbf{u} = \begin{bmatrix} \mathbf{u}_m \\ \mathbf{u}_s \end{bmatrix} = \begin{bmatrix} \mathbf{I} \\ -\mathbf{K}_{ss}^{-1}\mathbf{K}_{sm} \end{bmatrix} \mathbf{u}_m = \mathbf{R}\mathbf{u}_m. \tag{5}$$

Expressing the kinetic and the potential energy of the system in terms of $\mathbf{u}_m$ and using Lagrange's equation, we can obtain the equation of motion of the tension shadow mask with respect to the reduced degrees of freedom, $\mathbf{u}_m$, as

$$\mathbf{M}_m\ddot{\mathbf{u}}_m + \mathbf{K}_m\mathbf{u}_m = \mathbf{0}, \tag{6}$$

where

$$\begin{aligned}\mathbf{M}_m &= \mathbf{M}_{mm} - \mathbf{M}_{ms}\mathbf{K}_{ss}^{-1}\mathbf{K}_{sm} - \mathbf{K}_{ms}\mathbf{K}_{ss}^{-1}\mathbf{M}_{sm} + \mathbf{K}_{ms}\mathbf{K}_{ss}^{-1}\mathbf{M}_{ss}\mathbf{K}_{ss}^{-1}\mathbf{K}_{sm},\\ \mathbf{K}_m &= \mathbf{K}_{mm} - \mathbf{K}_{ms}\mathbf{K}_{ss}^{-1}\mathbf{K}_{sm}.\end{aligned} \tag{7}$$

Table 2 indicates that the errors in natural frequency of the lower modes computed using the reduced order model fall within 1%. It is mainly due to the fact that the z directional displacements of the shadow mask are indeed dominant.

Accounting for the damping and disturbance forces, Eq. (6) can be rewritten as

$$\mathbf{M}_m\ddot{\mathbf{u}}_m + \mathbf{C}_m\dot{\mathbf{u}}_m + \mathbf{K}_m\mathbf{u}_m = \mathbf{F}_m, \tag{8}$$

where $\mathbf{C}_m$ is the damping matrix and the disturbance force vector $\mathbf{F}_m = \mathbf{F}_C + \mathbf{F}_E$; $\mathbf{F}_C$ and $\mathbf{F}_E$ are the non-linear contact and external force vectors, respectively. The damping coefficient is normally determined by considering the experimental damping value of the shadow mask in vacuum CRT. In this work, it is assumed that $\mathbf{C}_m = \beta\mathbf{K}_m$, β being a constant, implying that higher modes are more heavily damped than lower modes [8,9].

3. Modelling of damping wire

The distributed mass of damping wire is lumped along the x direction at the nodes of the mask FE model to conveniently describe the contact interaction between wires and mask surface as shown in Fig. 5. The lumped masses are obtained as

$$m_i = \rho\frac{(\Delta s_{i-1} + \Delta s_i)}{2}, \tag{9}$$

where Δs_i is the ith element length and ρ is the mass per unit length of damping wire.Initial distributed contact force $f(x)$ of damping wire can be expressed as

$$f(x) = -T\frac{\partial^2 u(x)}{\partial x^2}, \tag{10}$$

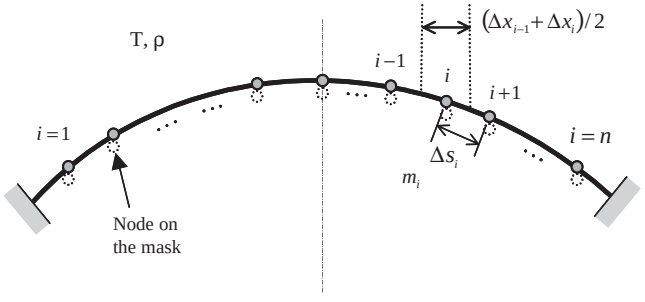

Fig. 5. Lumped parameter model of damping wire.

where T is the tension of the wire, and $u(x)$ is the displacement function of x in the z direction. Since Eq. (10) can be approximated as

$$F(x_i) = f(x_i) \cdot \Delta x_i = -\left.\frac{T(x)}{\Delta x}\right|_i \cdot \Delta u(x_i) = -k_i \cdot \Delta u(x_i), \tag{11}$$

where $\Delta u(x_i) = u(x_{i-1}) - 2u(x_i) + u(x_{i+1})$, and the lumped stiffnesses of damping wire can be expressed, assuming a uniform tension T along the wire, as

$$k_i = \left.\frac{T(x)}{\Delta x}\right|_i = \frac{T}{\Delta x_i}, \tag{12}$$

where Δx_i is the ith element length of damping wire along the x direction.

The mean m_i and k_i of the tested damping wire based on the mass per unit length of 1.35×10^{-5} kg/m and the tension of 130 gf, are about 1.85×10^{-5} kg and 200 N/m, respectively, and its fundamental natural frequency is 248 Hz.

4. Non-linear impact model

In order to examine the contact mechanism between the damping wire and the shadow mask plate, their $x - y$ planar motions in a resonant mode of the shadow mask were captured by using a high-speed camera. It was found that the measured motion of the damping wire of 30 μm in diameter on the $x - y$ plane relative to the mask is limited to 3–5 μm, whereas the z directional displacement is up to 100 μm. Thus, the impact in the z direction is considered to be the main source of interaction between the wire and the mask, the work done by friction being negligibly small.

When the shadow mask with non-uniform tension distribution, such as the V-shaped tension shadow mask of interest, resonates in a mode, its vibration mode is localized. On the other hand, the damping wire hardly vibrates, not resonating in the mask mode, and thus it tends to stand still in the air. This explains why the impact mechanism plays a major role in the interaction between the wire and the mask.

Contact problems are characterized by the constraints imposed on contact boundaries. In the treatment of contact constraints, two basic methods are available: the Lagrange multiplier method and the penalty method. The former method is not efficient to handle the structures with too many degrees of freedom such as the shadow mask system of interest, since it requires the inverse of stiffness matrix to obtain Lagrange multiplier in every computational time step [10–12]. The latter has been widely adopted in many commercial FE codes, but the determination of the penalty parameter depends on user's experience and trials and errors [10,13]. Therefore, we decided to introduce the contact–impact element composed of spring and damper in order to effectively describe the contact interactions, using the Hertzian contact theory and the concept of restitution coefficient.

4.1. Impact stiffness

The impact stiffness coefficient can be calculated using the Hertzian contact theory developed for two-cylinder case. Fig. 6 shows the two cylinders of length L, but with two different diameters D_1 and D_2, which are in contact under pressure P. The indentation length b can be obtained from the Hertzian contact theory as

$$b = 1.60\sqrt{pK_D C_E}, \tag{13}$$

where

$$p = P/L, \quad C_E = \frac{1-v_1^2}{E_1} + \frac{1-v_2^2}{E_2}$$

and $K_D = D_1 D_2/(D_1 + D_2)$. Here, the subscripts 1 and 2 represent cylinder 1 (shadow mask) and cylinder 2 (damping wire), respectively; E_i and v_i, $i = 1,2$, are the Young's modulus and the Poisson ratio, respectively. Since the compression of cylinder 1 along the axis of loading is given, for $E_1 = E_2$, $v_1 = v_2$ and $D_1 \gg D_2$, by [14,15]

$$\Delta u = \frac{2p(1-v^2)}{\pi E}\left(\frac{1}{3} + \ln\frac{2D_2}{b}\right) \tag{14}$$

the contact stiffness coefficient can be expressed as

$$K_c = \frac{\mathrm{d}p}{\mathrm{d}u}. \tag{15}$$

For the nominal tension level, 130 gf, of damping wire, K_c was determined to be 2.12×10^8 N/m. This extremely high value of K_c is due to the assumption of indentation of semi-infinite rigid body [15], causing an extraordinary computational burden.

4.2. Impact damping coefficient

The impact damping coefficient (C_c) can be calculated using the concept of restitution. Since the impedance of the damping wire (mass per unit length: 1.35×10^{-5} kg/m, diameter: 30 μm) is far

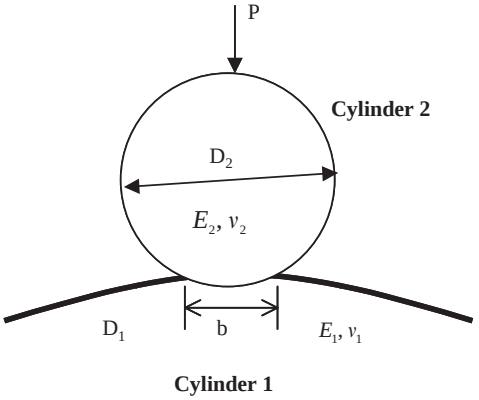

Fig. 6. Contact shape between two cylinders.

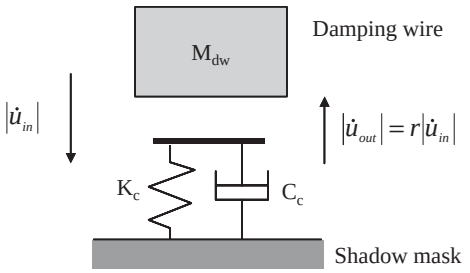

Fig. 7. Simple impact model to calculate the contact damping coefficient.

smaller than that of the shadow mask (mass per unit area: 0.595 kg/m^2, thickness: 0.1 mm), the shadow mask can be modelled as a spring–damper foundation system and each element of the damping wire as an impacted mass, as shown in Fig. 7. From this simplistic impact model, the equivalent damping coefficient can be easily estimated using the ratio between the velocities before and after on-set of impact. The restitution coefficient r is defined as

$$r = -\frac{\dot{u}(t_{out})}{\dot{u}(t_{in})} = \frac{|\dot{u}((1/2)\tau)|}{|\dot{u}(0)|} = e^{-\zeta\omega_n(\tau/2)}, \tag{16}$$

where $\dot{u}(t_{in})$ and $\dot{u}(t_{out})$ are the velocities of impacted mass before and after on-set of impact, respectively, and ω_n is the natural frequency of the spring–damper foundation during contact with the impacted mass, and τ is the period of motion of the spring–damper foundation.Using the relation $\omega_n\sqrt{1-\zeta^2}\cdot\tau = 2\pi$, the equivalent impact damping ratio in terms of the restitution coefficient r can be determined as

$$\zeta_r = \sqrt{\frac{(\ln r)^2}{\pi^2 + (\ln r)^2}}. \tag{17}$$

The impact damping coefficient (C_c) can then be expressed as

$$C_c = 2\zeta_r\sqrt{K_c M_{dw}}, \tag{18}$$

where M_{dw} is the lumped mass of damping wire element.

Now, we evaluate the computational accuracy and time in response calculations of the shadow mask with damping wires for the deduced impact stiffness and damping coefficients. Fig. 8 compares the effect of various contact stiffnesses on the response calculation at three selected points of the shadow mask with three damping wires for $r = 0.8$. The response points 1, 2 and 3 were selected at $(x, y) = (0, 0)$, (100,0) and (220,0), so that fundamental modal responses are well captured. Note that the contact stiffness K_c larger than 2.12×10^5 N/m has little influence on the computational accuracy of the mask displacement, although the computation time drastically increases. It takes about 18 h on a newest super computer to run a single simulation case with $K_c = 2.12 \times 10^8$ N/m for 1 s long results. Thus, we decided to use $K_c = 2.12 \times 10^5$ N/m for the simulation works, considering the computational efficiency as well as the computational accuracy.

Fig. 9 compares the effect of various contact damping coefficients on the response calculation of the shadow mask with damping wires for $K_c = 2.12 \times 10^5$ N/m. Note that, unlike the impact stiffness, variations in the impact damping coefficient C_c have little influence on the

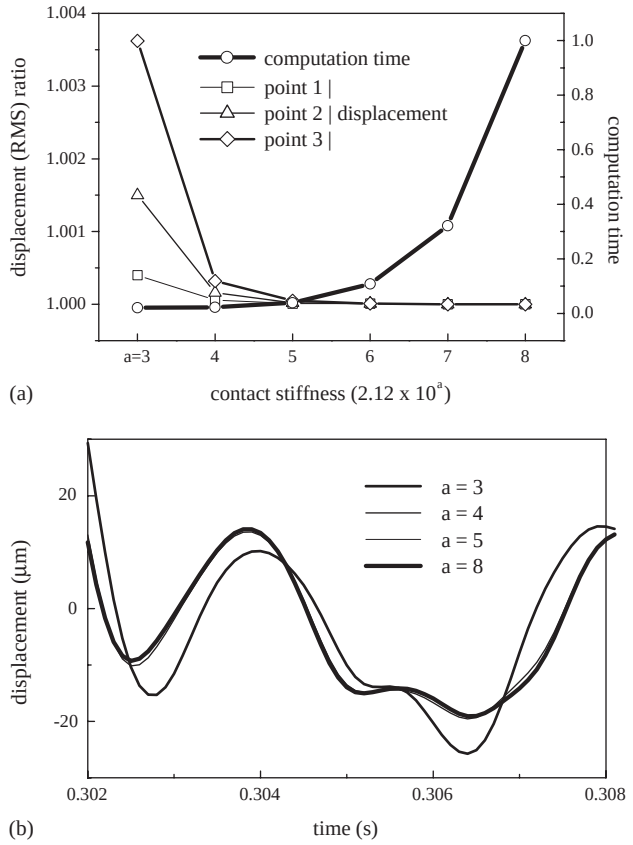

Fig. 8. Convergence characteristics with variation of the contact stiffness: (a) the convergence and computation time relative to the case of $K_c = 2.12 \times 10^8$ N/m and $r = 0.8$; (b) comparison of time responses.

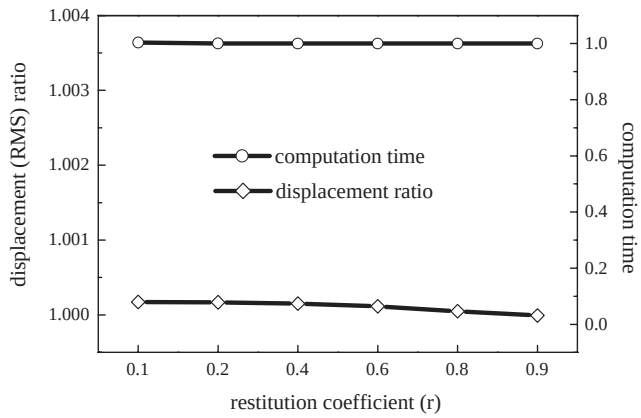

Fig. 9. Convergence characteristics with variation of the contact damping relative to the case of $r = 0.8$ and $K_c = 2.12 \times 10^5$ N/m.

computational accuracy and time. In the simulations, the typical value of $C_c = 0.887\,\mathrm{N\,s/m}$ was used, which corresponds to the case of $M_{dw} = 1.85 \times 10^{-7}\,\mathrm{kg}$ and $r = 0.8$ (steel balls) [16].

5. Non-linear vibration analysis

5.1. Initial displacements

The n dimensional displacement vector of the shadow mask and the l dimensional displacement vector of the damping wires can be written as, including the contactable and non-contactable elements,

$$\mathbf{u}_m = \{\, u_{m1} \quad u_{m2} \quad \cdots \quad u_{mi} \quad \cdots \quad u_{mq} \quad u_{m(q+1)} \quad u_{m(q+2)} \quad \cdots \quad u_{mj} \quad \cdots \quad u_{mn} \,\}^{\mathrm{T}}, \tag{19}$$

$$\mathbf{u}_d = \{\, u_{d1} \quad u_{d2} \quad \cdots \quad u_{di} \quad \cdots \quad u_{dq} \quad u_{d(q+1)} \quad u_{d(q+2)} \quad \cdots \quad u_{dj} \quad \cdots \quad u_{dl} \,\}^{\mathrm{T}}, \tag{20}$$

where the subscripts m and d indicate the shadow mask and damping wire, respectively, and q is the total number of contactable degrees of freedom of the shadow mask and damping wires.

The initial displacements of the shadow mask and damping wires to the initial assembling forces, which can be calculated by the analysis of static deformation, are denoted as

$$\mathbf{u}_m|_{t=0} = \{\, \delta_{m1} \quad \cdots \quad \delta_{mi} \quad \cdots \quad \delta_{mn} \,\}^{\mathrm{T}}, \tag{21}$$

$$\mathbf{u}_d|_{\mathrm{t}=0} = \{\, \delta_{d1} \quad \cdots \quad \delta_{di} \quad \cdots \quad \delta_{dl} \,\}^{\mathrm{T}}. \tag{22}$$

On the other hand, the initial compression δ_{ci} of the ith element, having the contact stiffness K_{ci}, can be obtained as

$$\delta_{ci} = \frac{F_{0i}}{K_{ci}}, \qquad i = 1, 2, \ldots, q, \tag{23}$$

where F_{oi} is the corresponding contact force.The equations of motion of the assembled system can then be written as

$$\mathbf{M}_m\ddot{\mathbf{u}}_m + \mathbf{C}_m\dot{\mathbf{u}}_m + \mathbf{K}_m\mathbf{u}_m = \mathbf{F}_m, \tag{24}$$

$$\mathbf{M}_d\ddot{\mathbf{u}}_d + \mathbf{C}_d\dot{\mathbf{u}}_d + \mathbf{K}_d\mathbf{u}_d = \mathbf{F}_d, \tag{25}$$

where $\mathbf{F}_m$ is the force vector to the shadow mask, which is composed of the non-linear contact forces ($\mathbf{F}_C$) at contactable points and the external forces ($\mathbf{F}_E$) given by

$$\mathbf{F}_m = \mathbf{F}_C + \mathbf{F}_E = \{\, F_{C1} \quad F_{C2} \quad \cdots \quad F_{Ci} \quad \cdots \quad F_{Cq} \quad 0 \quad 0 \quad \cdots \quad 0 \,\}_n^{\mathrm{T}} + \mathbf{F}_E, \tag{26}$$

where F_{Ci}, the contact force acting on the ith contact point of the shadow mask, is given by

$$F_{Ci} = \begin{cases} K_{ci}[(u_{di} - \delta_{di}) - (u_{mi} - \delta_{mi}) + \delta_{ci}] + C_{ci}(\dot{u}_{di} - \dot{u}_{mi}) & \text{for } u_{di} - u_{mi} > \delta_{di} - \delta_{mi} - \delta_{ci}\ \text{(contact)} \\ 0 & \text{otherwise (non-contact)} \end{cases}. \tag{27}$$

The force $\mathbf{F}_d$ acting to damping wires reacts against the non-zero elements of $\mathbf{F}_C$, i.e.,

$$\mathbf{F}_d = \{\, -F_{C1} \quad -F_{C2} \quad \cdots \quad -F_{Ci} \quad \cdots \quad -F_{Cq} \quad 0 \quad 0 \quad \cdots \quad 0 \,\}_l^{\mathrm{T}}. \tag{28}$$

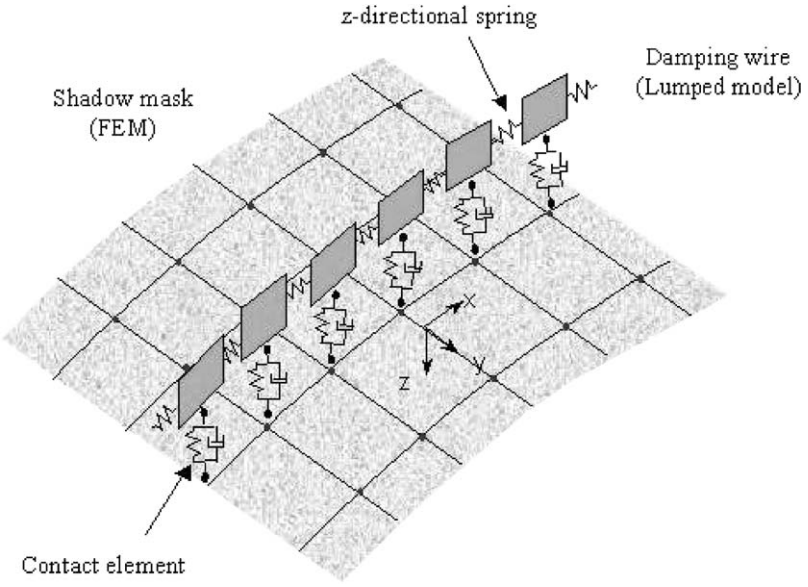

Fig. 10. Analysis model of the shadow mask and damping wire.

Fig. 10 shows the analysis model of the shadow mask system, including the damping wire and contact elements.

5.2. Non-linear vibration analysis

Fig. 11 shows the typical relative displacement and velocity, and the contact spring and damping forces at a contact point calculated from the non-linear vibration analysis, when the shadow mask is excited by a half-sine impact. The thick solid line in Fig. 11(a) indicates the relative displacement between the mask and the damping wire at a pair of mating contact points; positive (negative) value means contact (no contact) between them. When they are in contact, the contact spring force, which is defined as the penetrated displacement times the contact stiffness coefficient, remains positive; otherwise, it vanishes. The contact damping force, which is defined as the penetration rate times the contact damping coefficient, tends to become large at the on-set of contact, due to the relatively large velocity, as shown in Fig. 11(b).

6. Experimental verification of the analysis model

Because the tension shadow mask is a thin tension plate with many small holes, its dynamic characteristics can be greatly affected by aerodynamic damping in the air. For fair comparison of the analytical and experimental results, we constructed a vacuum test chamber to simulate the commercial CRT environment, as shown in Fig. 12.

To perform the impact tests for the shadow mask placed in the vacuum test chamber, a pendulum type impact hammer is designed to excite the shadow mask such that the thread, which

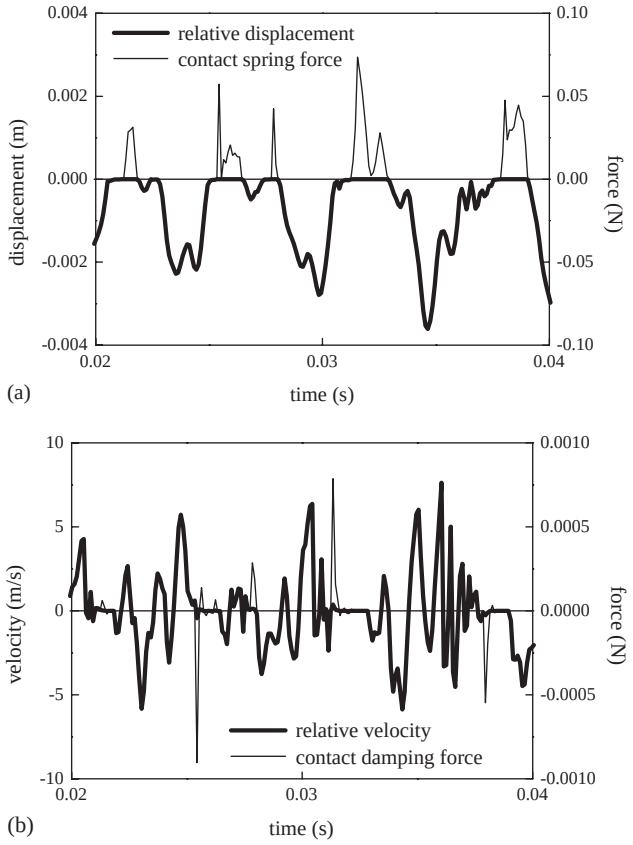

Fig. 11. Relative vibration responses and contact forces at a contact point.

initially holds the pendulum against the gravity, is burned by an outside heat source and thus the pendulum is released. The responses of the shadow mask in the vacuum chamber are measured using a laser Doppler vibrometer through the sensing window, as shown in Fig. 12. The excitation and measurement points on the shadow mask are marked in Fig. 13. Note that the excitation point was carefully selected to equally well excite the fundamental and second modes.

Fig. 14(b) compares the measured and estimated time histories of the shadow mask without damping wires obtained by using the measured impact force in Fig. 14(a) as the input force. It shows that they are in good agreement with each other, confirming the validity of the linear analysis model of shadow mask without damping wires.

Fig. 15(a) shows the measured impact force, which is then used as the input force to calculate the analytical response of the shadow mask with three damping wires. Fig. 15(b) compares the measured and estimated response spectra, which are also in good agreement for the case with three damping wires. Note that the effect of damping wires on the response spectrum is significant. Fig. 15(c) and (d) show the corresponding time histories, which again confirm the previous observations. It can be concluded here that the analysis model can well describe the non-linear vibration characteristics of the shadow mask with the damping wires.

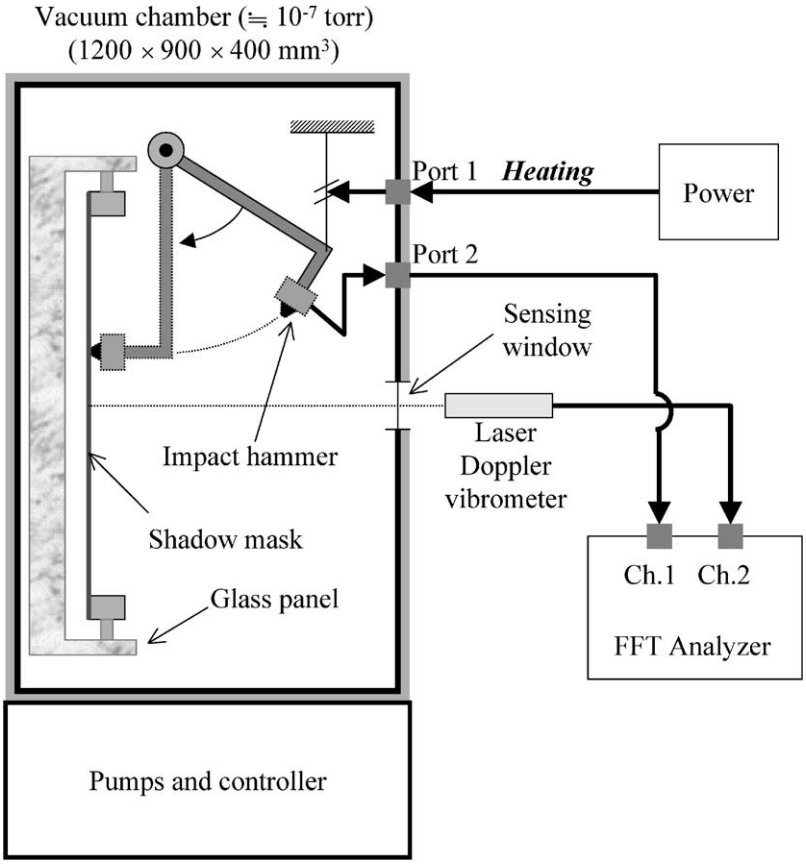

Fig. 12. Experimental set-up.

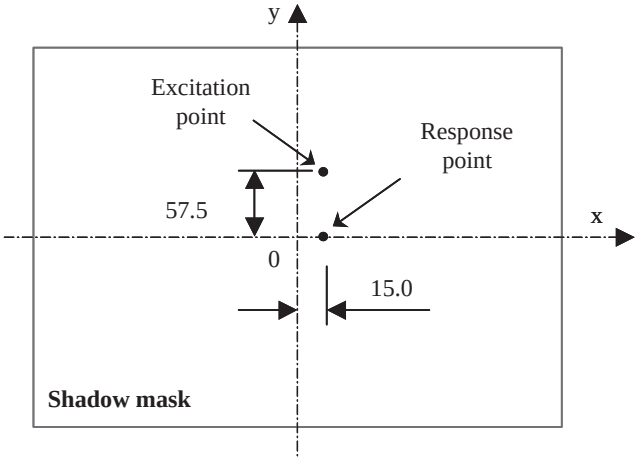

Fig. 13. Measuring points of excitation and response on the shadow mask.

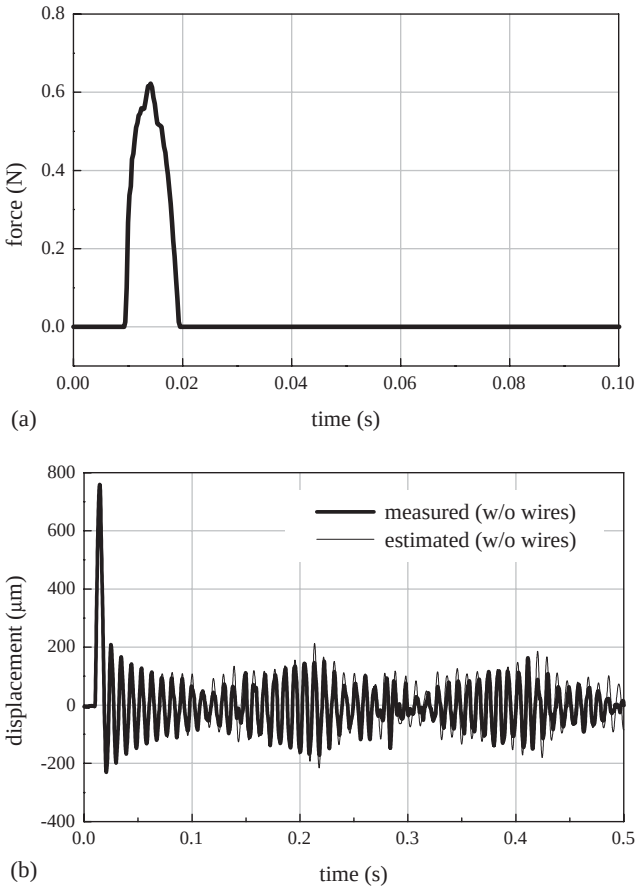

Fig. 14. Comparison of the measured and estimated responses of the shadow mask without damping wires: (a) input force (measured impact force); and (b) time histories.

7. Effects of design parameters of damping wires

In the design stage of shadow mask, some design parameters associated with damping wires are considered to be important, as shown in Fig. 16 and summarized in Table 3. They are the number of damping wires (n_w), the tension of damping wire (T), the separation distance of damping wires (Δy) and the fixing positions of damping wires relative to the edge line of the shadow mask (Δx, Δz). The tension parameter of damping wire is replaced by its natural frequency ratio (r_t) to the shadow mask, i.e., $r_t = f_{d1}/f_{m1}$, where f_{d1} and f_{m1} are the fundamental natural frequencies of damping wire and shadow mask without damping wires, respectively. The reference design parameters are set to be $f_{m1} = 106\,\text{Hz}$, $y_0 = 460\,\text{mm}$, $\Delta y_0 = y_0/4 = 115\,\text{mm}$, $\Delta x_0 = 2.5\,\text{mm}$ and $\Delta z_0 = 0.0\,mm$. In the simulations, the shadow mask is excited at its center point by a half-sine impact to get its vibration characteristics. The duration and amplitude of the impact are 10 ms and 0.5 G, respectively. The calculated responses at $(x, y) = (0, 0)$, (100,0) and (220,0) along the x-axis of the mask were used to evaluate the vibration reduction with the design parameters varied. For

the performance index, the root mean square (r.m.s.) response for the initial 10 s, $z_{r.m.s.}$, was used and the Taguchi method [17] developed for design of experiments was employed to effectively search for an optimal parameter design.

Fig. 17 is the plot of parameter effects on $z_{r.m.s.}$. It implies that the tension and the number of damping wires, that mainly increase the stiffness of tension shadow mask, are the significant design parameters and that the variations in Δx, Δy and Δz, if not too large, hardly affect the vibration attenuation of the shadow mask. The case with $n_w = 3$, $r_t = 1.3$, $\Delta y = \Delta y_0$, $\Delta x = 2\Delta x_0$ and $\Delta z = -2$ mm is considered to be the candidate for best performance.

A confirmation run, which is widely adopted in Taguchi method to check the reproducibility of results, was conducted using the optimal levels for each design parameters and the result was compared with the predicted value. Predicted values of $z_{r.m.s.}$ were found to be 46.05 and 45.52 μm, respectively, for the case only with two optimal major parameters, $n_w = 3$ and $r_t = 1.3$, and for the case with all optimal parameters. On the other hand, the simulation for the confirmation run led

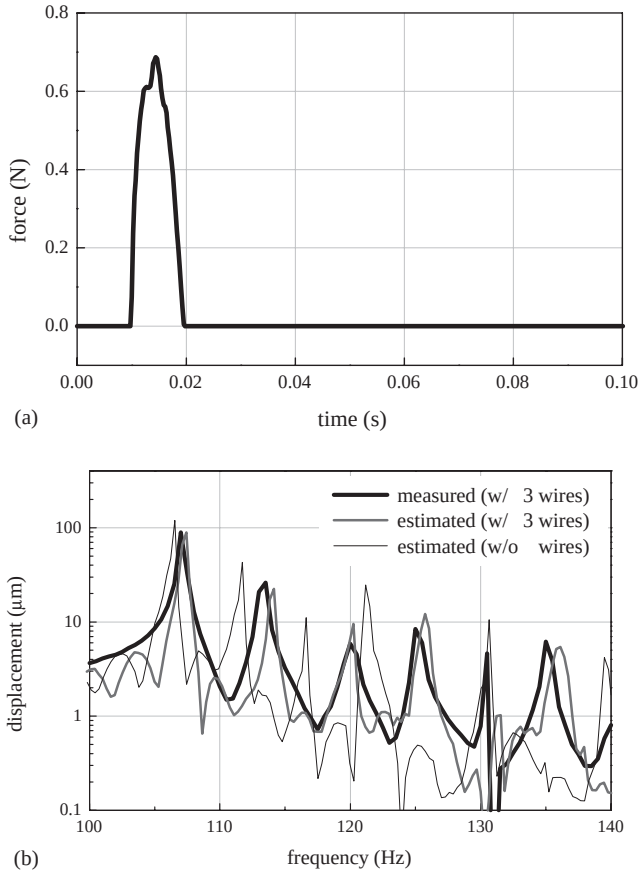

Fig. 15. Comparison of the measured and estimated responses of the shadow mask with and without damping wires: (a) input force (measured impact force), (b) response spectra, (c) time history with three wires; and (d) estimated time history without wires.

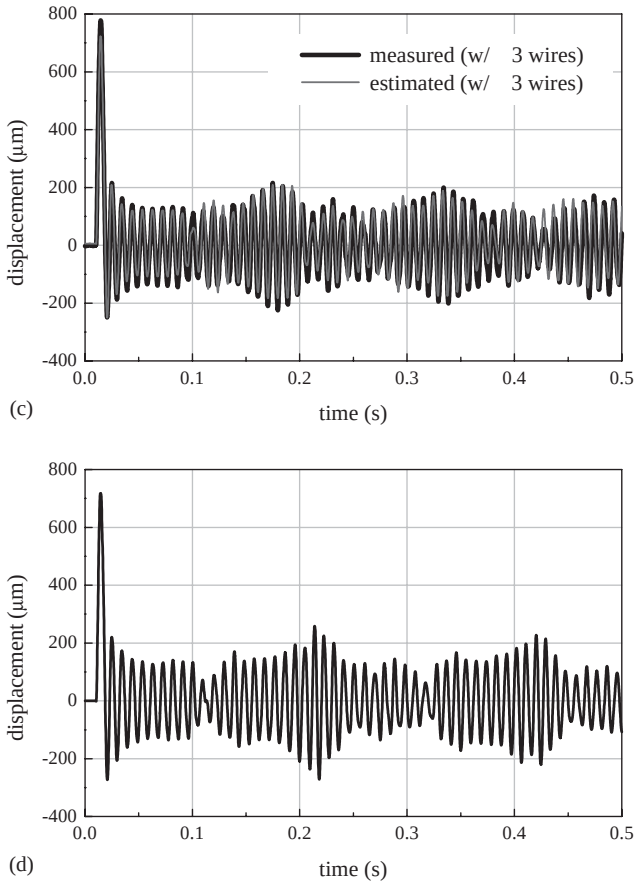

Fig. 15 (*continued*).

to $z_{r.m.s.} = 45.22\,\mu m$, which is in good agreement with the predictions. In conclusion, the pronounced sensitivity of the number and the tension of damping wires to $z_{r.m.s.}$ has been well justified.

Note that the efficiency of vibration reduction is nearly proportional to the natural frequency of the damping wire. On the contrary, it has been reported that, for the flat uniform tension shadow mask, the worst performance is expected when the natural frequency of the damping wire coincides with that of the shadow mask [6,18].

Fig. 18 compares the time responses of the shadow mask at its center (point 1) without damping wires and with the optimally tuned damping wires. Close examination of the vibration reduction rates up to 10 s indicates that the efficiency of vibration reduction due to introduction of the optimized damping wires increases by 33% at point 1, 41% at point 2 and 50% at point 3, compared with the mask without damping wires. On the other hand, the performance index, $z_{r.m.s.}$, which is the vibration reduction efficiency in terms of the RMS response for the initial 10 seconds, was decreased by 13% at point 1, 19% at point 2, and 28% at point 3, respectively.

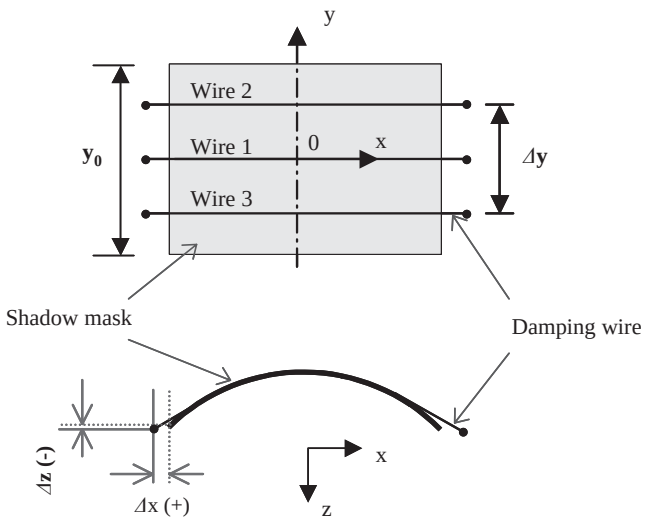

Fig. 16. Design parameters of damping wire.

Table 3
Design parameters of damping wires

Level	n_w	r_t	$\Delta y/\Delta y_0$	$\Delta x/\Delta x_0$	Δz
1	3	1.3	2	2	0
2	2	1.0	1	1	−2 mm
3	1	0.7			

$r_t = f_{d1}/f_{m1}$, $\Delta y_0 = y_0/4$, $\Delta x_0 = 2.5$ mm, $\Delta z_0 = 0$ mm.

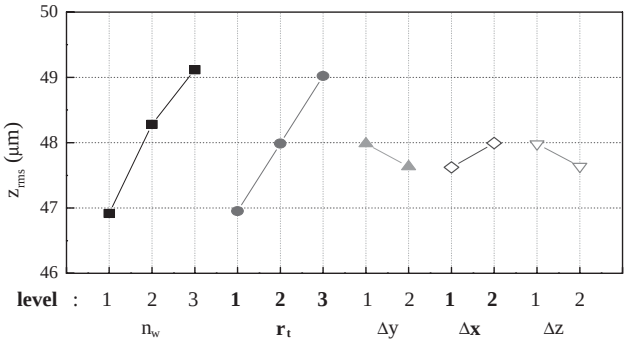

Fig. 17. Plot of parameter effects.

8. Conclusion

The reduced order dynamic model of the tension shadow mask was developed using a commercial FEM code, and the lumped parameter model of damping wire was used to easily

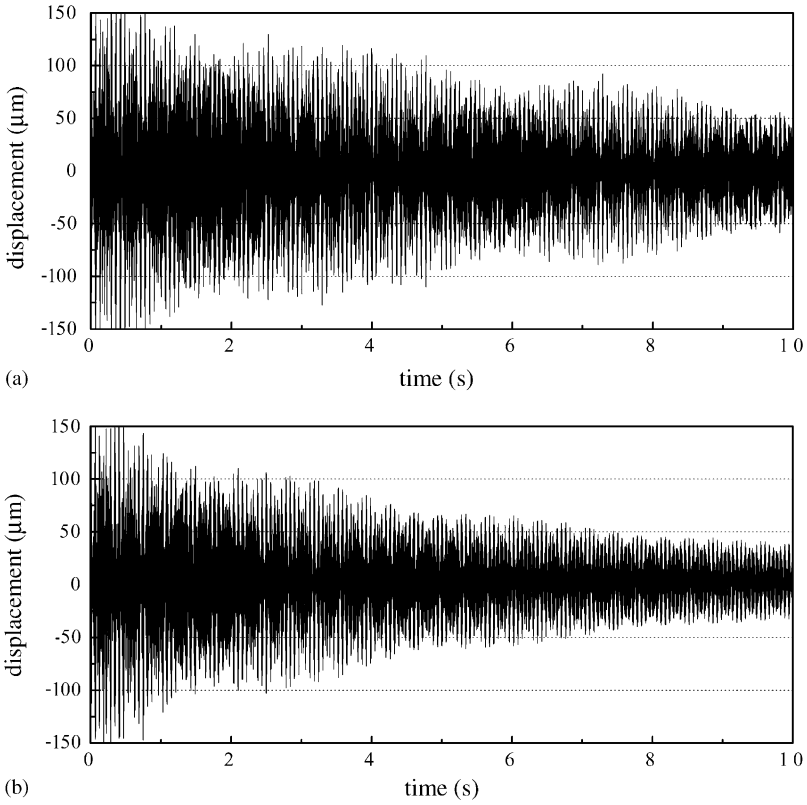

Fig. 18. Time response at point 1 of the shadow mask: (a) without damping wires and (b) with the optimally tuned damping wires.

describe the contact interactions with the shadow mask. Non-linear contact–impact mechanism composed of spring and damper elements was introduced to describe the interaction of the shadow mask and damping wire. The spring and damper constants were determined using the Hertzian contact theory and the concept of restitution coefficient, respectively. Impact tests of shadow masks in a vacuum chamber were successfully carried out so that the modelling scheme was validated with fair accuracy. Using the verified analysis model, parametric study with the damping wire design parameters varied was performed based on the Taguchi method, in order to evaluate the parameter effects on the impulse response of the shadow mask. It was found that the tension and the number of damping wires are the most significant parameters. The results of the parametric study suggested that the optimized damping wires can reduce the vibration of the shadow mask by 30–50% compared with the case without damping wires.

References

[1] Shadow mask for CRT, Japan Patent 10-308182.
[2] M. Watanabe, H. Suzuki, New vibration prevention system of shadow mask for flat type CRT, 2000 SID (Society for Information Display) Conference, 2000, pp. 1245–1247.

[3] Y. Ohmura, M. Hashimoto, H. Taguchi, Effect of damping wire on aperture grill vibration, IDW '99, pp.481-484.
[4] Shadow mask for CRT, Japan Patent 10-302665.
[5] Shadow mask for CRT, Japan Patent 10-172449.
[6] S.J. You, W.S. Shin, B.W. Jang, An analysis of a mask vibration considering contact with a damping wire, IEEE Transactions on Consumer Electronics 46 (2) (2000) 385–389.
[7] H.G. Kim, Thermal deformation analysis of a shadow mask, Master's Thesis, Korea Advanced Institute of Science and Technology (KAIST), 1993.
[8] M. Petyt, Introduction to Finite Element Vibration Analysis, Cambridge Universal Press, Cambridge, 1990.
[9] K.J. Bathe, Finite Element Procedures in Engineering Analysis, Prentice-Hall, Englewood Cliffs, NJ, 1982.
[10] Z.H. Zhong, Finite Element Procedures for Contact–Impact Problems, Oxford University Press, Oxford, 1993.
[11] F. Collombet, X. Lalbin, J. Bonni, J.L. Lataillade, Contact impact techniques for the study of impact laminated structures, Mathematical and Computer Modeling 28 (4-8) (1998) 171–184.
[12] T.M. Wasfy, A.K. Noor, Computational procedure for simulating the contact/impact response in flexible multi-body system, Computer Methods in Applied Mechanics and Engineering 147 (1997) 153–166.
[13] User's manual of 'Penalty contact' in ABAQUS/Explicit.
[14] R.J. Roask, W.C. Young, Formulas for Stress and Strain, McGraw-Hill, New York, 1976.
[15] S.P. Timoshenko, J.N. Goodier, Theory of Elasticity, 3rd Edition, McGraw-Hill, New York, 1982.
[16] A. Higdon, Engineering Mechanics, Prentice-Hall, Englewood Cliffs, NJ, 1979.
[17] M.S. Phadke, Quality Engineering Using Robust Design,, Prentice-Hall, Englewood Cliffs, NJ, 1989.
[18] S.D. Kim, Damper wire for shadow mask in flat Braun tube, Application number of US patent 09/689,869, 1999.